Draft version November 6, 2023
Typeset using LaTeX **preprint** style in AASTeX631

Inferring the redshift of more than 200 GRBs with a Machine Learning Ensemble model

Maria giovanna Dainotti,[1, 2, 3, 4, 5] Elias Taira,[6] Eric Wang,[7] Elias Lehman,[8]
Aditya Narendra*,[9, 10] Grzegorz M. Madejski,[11] Vahe Petrosian,[11] Agnieszka Pollo,[12, 10]
Malgorzata Bogdan,[13, 14] and Apratim Dey[15]

[1] *Division of Science, National Astronomical Observatory of Japan, 2-21-1 Osawa, Mitaka, Tokyo 181-8588, Japan*
[2] *The Graduate University for Advanced Studies (SOKENDAI), Shonankokusaimura, Hayama, Miura District, Kanagawa 240-0115*
[3] *Space Science Institute, 4765 Walnut St Ste B, Boulder, CO 80301, USA.*
[4] *Nevada Center for Astrophysics, University of Nevada, 4505 Maryland Parkway, Las Vegas, NV 89154, USA*
[5] *Bay Environmental Institute, P.O. Box 25 Moffett Field, CA, California*
[6] *Department of Physics and Astronomy, Michigan State University, East Lansing, MI 48825, USA*
[7] *Department of Computer Science, Yale University, New Haven, CT 06511-8937*
[8] *Department of Physics, University of California at Berkeley, Berkeley, CA 94720, USA*
[9] *Jagiellonian University, Doctoral School of Exact and Natural Sciences, Krakow, Poland*
[10] *Astronomical Observatory of Jagiellonian University, Krakow, Poland**
[11] *Department of Physics and SLAC National Accelerator Laboratory, Stanford University, Stanford, CA 94305, USA*
[12] *National Center for Nuclear Physics (NCB), Warsaw*
[13] *Department of Mathematics, University of Wroclaw, 50-384, Poland*
[14] *Department of Statistics, Lund University, SE-221 00 Lund, Sweden*
[15] *Department of Statistics, Stanford University, Stanford, CA, 94305, USA*

(Dated: July 2023)

ABSTRACT

Gamma-ray bursts (GRBs), due to their high luminosities are detected up to redshift 10, and thus have the potential to be vital cosmological probes of early processes in the universe. Fulfilling this potential requires a large sample of GRBs with known redshifts, but due to observational limitations, only 11% have known redshifts (z). There have been numerous attempts to estimate redshifts via correlation studies, most of which have led to inaccurate predictions. To overcome this, we estimated GRB redshift via an ensemble supervised machine learning model that uses X-ray afterglows of long-duration GRBs observed by the Neil Gehrels Swift Observatory. The estimated redshifts are strongly correlated (a Pearson coefficient of 0.93 in $\log(z+1)$ scale) and have a root mean square error, namely the square root of the average squared error $\langle \Delta z^2 \rangle$, of 0.46 with the observed redshifts showing the reliability of this method. The addition of afterglow parameters improves the predictions considerably 63% compared to previous results in peer-reviewed literature. We finally use our ML method to infer the redshifts of 208 GRBs which increase the known redshifts of long GRBs with plateaus by 94%, a significant milestone for enhancing GRB population studies which requires large samples with redshift.

1. INTRODUCTION

Gamma-Ray Bursts (GRBs) are the most luminous events after the Big Bang. Due to their high luminosities, they are detected up to redshift $z = 9.4$ (Cucchiara et al. 2011), and thus have the potential to be vital cosmological probes of processes in the early universe. Studying GRBs enables us to deepen our knowledge about the early universe and track how the universe evolves over time since GRB redshift range goes from 0.0085 (Galama et al. 1998)) to the highest redshifts observed (between 8 and 9.4, (Cucchiara et al. 2011; Tanvir et al. 2008). GRBs, (observed mainly in γ-rays, X-rays, and sometimes in optical) are traditionally classified in short duration, SGRBs, with $T_{90} < 2$ s, where T_{90} is the time interval during which the GRB emits 90% of its total observed fluence (energy emitted in gamma-rays) and long duration, LGRBs, where $T_{90} > 2$ s. Observationally, GRBs are characterized by prompt emission, the main emission observed from hard X-rays to high-energy -rays and sometimes in optical (Vestrand et al. 2005; Beskin et al. 2010; Gorbovskoy et al. 2012; Vestrand et al. 2014), and the afterglow emission (Costa et al. 1997; van Paradijs et al. 1997; Piro et al. 1998), a long-lasting multi-wavelength emission, following the prompt, observed in X-rays, optical, and sometimes radio. The afterglow sometimes contains the plateau emission feature where the flux during the plateau remains constant (Nousek et al. 2006; Rowlinson et al. 2014; Zhang et al. 2006; Dainotti et al. 2008; Sakamoto et al. 2007; O'Brien et al. 2006; Zaninoni et al. 2013; Liang et al. 2007). Plateaus are observed in 42% of X-ray afterglows (Evans et al. 2009; Li et al. 2018) and in 30% of optical afterglows (Vestrand et al. 2005; Kann et al. 2006; Zeh et al. 2006; Dainotti et al. 2020; Panaitescu & Vestrand 2008, 2011; Oates et al. 2012).

Currently, the main issue in general in population studies is the lack of LGRB samples with known redshifts. The direct determination of the redshift of a GRB requires rapid localization and spectral information. One of the most powerful observatories that enables rapid detection and follow-up in multiwavelengths is the Neil Gerhels Swift observatory (hereafter Swift) (Gehrels et al. 2004). Swift uses an X-ray instrument for localization and can obtain spectra and sometimes redshift with the on-board UVOT instrument. The Swift satellite consists of three main instruments: the Burst Alert Telescope (BAT) (Burrows et al. 2005), the X-ray Telescope (XRT) (Barthelmy et al. 2005), and the Ultraviolet/Optical Telescope (UVOT) (Roming et al. 2005). These instruments work together to detect, localize, and collect data on GRBs and their afterglows across various wavelengths including gamma-rays, X-rays, and ultraviolet/optical.

Swift, with its localization capabilities, has paved the way to the high-z Universe. Despite all the advantages of localization provided by Swift, still, only 26.2% (420) of Swift's 1604 GRBs have known spectroscopic redshifts up to today date (23rd of August 2023). Redshift measurements, particularly high-z ones, are challenging due to limited telescope time and the paucity of active GRB follow-up programs. Thus, efforts to determine the redshift of GRBs are of paramount importance.

One of the key goals of increasing the sample of GRBs with known redshift is to determine an accurate measure of the luminosity function (LF), which provides the number of bursts per unit luminosity, key to understanding the properties of GRB luminosities as a population, the energy release and emission mechanism of GRBs. Another relevant goal is the determination of the cosmic GRB formation rate (GRBFR), which provides the number of events per comoving volume and time, pivotal to understanding the production of GRBs at various stages of the universe. As highlighted

[*] E-mail: aditya.narendra@doctoral.uj.edu.pl

in Petrosian et al. (2015), there exists a discrepancy between LGRBs compared to the overall rates of star formation within the lower redshift range ($0 < z < 1$). This result has been found by several groups with differences and thus the debate is still open. Obtaining more redshifts becomes crucial for settling such a debate.

Another great advantage of having more GRBs with redshift is the possibility of using GRBs as standardized candles with empirical relations between distance-dependent and intrinsic properties of GRBs. Amongst the earliest of these efforts, is the Dainotti Relation (Dainotti et al. 2008, 2011, 2015; Dainotti et al. 2017), a roughly inversely proportional relationship between the rest-frame time at the end of the plateau phase ($T_a/(1+z)$) and its corresponding luminosity (L_a). Later Dainotti et al. (2013) showed that via the use of the Efron and Petrosian method (Efron & Petrosian (1992)) this relation is intrinsic and not due to selection biases. This relation has also been discovered in the optical and radio emission (Dainotti et al. 2020; Levine et al. 2022). It has also been extended in three dimensions in X-rays, where the peak prompt luminosity L_{peak} has been added to the two-dimensional Dainotti relation (Dainotti et al. 2016, 2017; Dainotti et al. 2020). In addition, GRBs observed by Fermi-LAT and detailed in the Second Fermi GRB Catalog (Ajello et al. 2019), which show the existence of the plateau in γ-rays, obey this correlation as well (Dainotti et al. 2021). Continuing on the extension of this relation in other wavelengths, this three-dimensional relation has been found in optical too Dainotti et al. (2022a).

Both the two and three-dimensional relations have been used as a valuable cosmological tool (Cardone et al. 2009, 2010; Dainotti et al. 2013; Postnikov et al. 2014; Cao et al. 2021, 2022a,b; Dainotti et al. 2022b; Dainotti et al. 2023; Bargiacchi et al. 2023; Dainotti et al. 2023). Dainotti et al. (2022b), showed how the Dainotti relation used in combination with SNe Ia is able to obtain consistent results on matter density, Ω_M to SNe Ia in the ΛCDM model with the added benefit of extending the distance ladder up to $z = 5$, a redshift far greater than the farthest observed SNe Ia observed up until $z = 2.26$ (Rodney & Riess 2015). Another large part of this paper discussed the prediction of the number of GRB observations that we would need to obtain the same precision as SNe Ia on the matter density, Ω_M in the ΛCDM model as in Conley et al. (2011); Betoule et al. (2014); Scolnic et al. (2018).

Indeed, it has been discussed in Dainotti et al. (2022c) that we need 789 GRBs to reach the same precision of SNe Ia in Conley et al. (2011). Thus, we need to add 567 more GRBs to our current sample of 222 GRBs with X-ray plateaus and known redshift.

To increase the number of GRBs with redshifts, there have been several attempts in this direction by finding correlations between distance-independent quantities (peak flux, duration of afterglow plateau, as the already mentioned Dainotti et al. (2008); Dainotti et al. (2013), etc) and distance-dependent GRB properties (prompt emission peak luminosity) to find pseudo-redshifts for the GRBs with unknown redshift (Atteia (2003), Yonetoku et al. (2004), Dainotti et al. (2011)). The results of these analyses are all reliant on the luminosity distance (D_L), a quantity that by definition, not only depends on cosmology but small variations of the D_L at high redshift are subject to large variations of the redshift. Thus, these results are inherently subject to inaccuracy. To avoid the issues caused by including D_L in the current of determining pseudo-redshifts, we undergo here a new approach that relies on the use of ML algorithms to create our redshift predictions.

The paper is structured as follows: in Sec. 1 we detail the problem of paucity of the redshifts, in Sec. 2 we describe the dataset. In Sec. 3, we describe our pipeline from how we process our data to select the variables to be used to how we build and test our models on our data. In Sec. 4 we discuss the performance of our model as well the predictions on the generalization set and we compare those results to the distribution of the existing set of redshifts. Finally in Sec. 5 we summarize and discuss the implications of these results.

2. THE DATA SAMPLE

In this study, we focus on GRBs observed in gamma-rays and X-rays detected by the BAT and the XRT telescopes onboard the Swift. We used the data stored in the NASA Swift GRB Search Tool, and the Third Swift-BAT GRB Catalogue (Lien et al. 2016). Our initial step involves preprocessing the raw GRB data to ensure its quality and suitability for further analysis. Considering the distinct nature of various GRB classes, such as LGRBs and SGRBs, which can originate from different progenitors or the same progenitors in diverse environments, it is crucial to avoid blending the characteristics of these diverse classes. For this reason, our study focuses only on LGRBs. Thus, we exclude from our sample, taken from Dainotti et al. (2020) and Srinivasaragavan et al. (2020), SGRBs, SGRBs with extended emission (Norris & Bonnell 2006) and the intrinsically SGRBs which have $T_{90}/(1+z) < 2$s. The initially available features are the following:

1. T_{90} - the time interval during which the GRB emits 90% of its total observed fluence (energy emitted in gamma-rays).
2. F_a - the flux at the end of the plateau emission.
3. T_a - the time at the end of the plateau emission.
4. α - the temporal power-law index after the end of the plateau emission.
5. β - the spectral index assuming a power-law for the spectral energy distribution in the range of the plateau emission.
6. γ - the spectral index in the prompt emission assuming a power-law for the spectral energy distribution.
7. Fluence - the energy fluence over T_{90} of the prompt emission in units of erg $^{-2}$.
8. PhotonIndex - the prompt photon index of the photon energy distribution modeled with a simple power law.
9. NH - The column density of neutral hydrogen along the line of sight.
10. Peak Flux - The prompt peak photon flux in units of with unit of (number of photons) cm^{-2} s^{-1}.

The dataset with which we train and test our ML models contains 222 GRBs with all the features listed above, called the predictors, as well as our response variable, the redshift. Furthermore, as mentioned in Sec. 1, there are also 208 GRBs without a measured redshift and the same features. This set is called the generalization set. The ML models are used to predict the redshift of these GRBs.

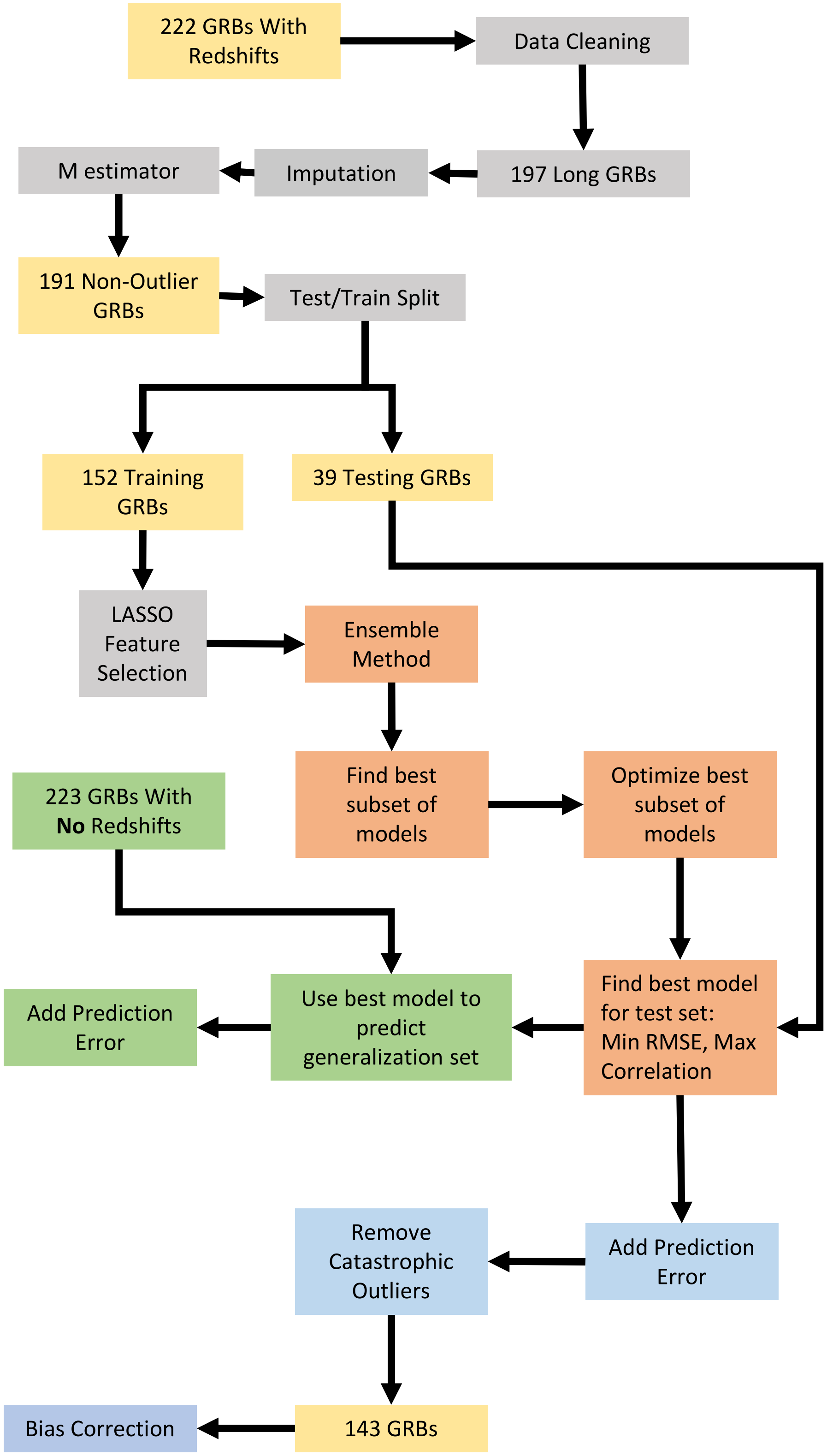

Figure 1. The flowchart detailing each step of the pipeline. All yellow boxes represent indicate the number of GRBs in the training set at each step of the process. Grey boxes are pre-processing steps. Orange boxes indicate all steps involving model construction. Green boxes show all steps involving the generalization set predictions. Blue boxes show all the post-processing steps with the training set

3. METHODOLOGY

Fig. 1 shows the summarized flowchart for our methodology. The individual parts are expanded upon in the following subsections.

3.1. *Data Cleaning and Transformation*

Due to the wide range encompassed by specific variables, namely Peak Flux, T_a, Fluence, NH, T_{90}, and F_a, we transformed these variables into log base-10 with the aim of enhancing prediction accuracy. The variables, α, β, and γ, Photon Index remain in the linear scale since the range in which they vary is of the order of unity. We then proceed to clean our data such that we exclude any non-physical values from our analysis or values which are unusual for the majority of GRBs such as $\alpha > 3$, $\beta > 3$, $\gamma > 3$, Photon Index < 0 so that we can capture the average feature of GRBs. All $\log(NH) < 20$ are considered to be nonphysical and are thus set to NA and then imputed (see Sec. 3.2). We also perform a similar transformation to our redshifts in which we create the new response variable $\log(1 + z)$. This results in a Gaussian distribution with a mean=0.48 and a standard deviation=0.128 for this response variable, rather than a distribution with tails as shown for the distribution of the redshift in the scatter matrix plot of Fig. 2. This new response variable is chosen similarly as in previous literature (Dainotti et al. (2021), Gibson et al. (2022), Narendra et al. (2022)), and it is a natural choice since it mimics the evolution of the variables. In addition, z+1 is a more natural parametrization of the cosmological variable z. We show the scatter matrix plot after the data cleaning and transformation, see Fig. 2.

3.2. *Data Imputation: MICE*

Multiple Imputation by Chained Equations (MICE) can impute missing values for multiple variables using variables from the data set that are complete. MICE has the ability to create imputed values in R with a variety of different methods. Here we use a predictive mean-matching method known as “midastouch” to create our model. We employ the “midastouch” approach, a predictive mean matching (PMM) technique introduced by Little & Rubin (2019). This method begins by populating missing values in a feature with its mean and subsequently estimating these values by training a model on the available complete data. For each prediction, a probability is assigned based on its distance from the value imputed for the missing variable. The missing entry is imputed by randomly drawing from the observed values of the respective predictor, weighted according to the probability defined previously.

This process is then repeated N times, after which, the final substituted quantity for each missing value is determined by taking an average over the prediction of the value in each iteration.

In previous literature, like in Gibson et al. (2022), similar methodologies have been applied to Active Galactic Nuclei data from the Fermi Fourth LAT catalog with no noticeable addition to the uncertainty of the resulting data distribution. In fact, the constructed ML strictly benefits from its application due to the increased size of the dataset. Given that GRBs also exhibit similarly nonlinear trends within their features, we expect we should see similar results in our own study.

Here we show the missing data in Fig. 3. The bottom x-axis shows the number of missing GRBs corresponding to the variable presented in the upper x-axis. The pink boxes show the missing GRB variables, while the blue boxes indicate GRBs with no missing data for given variables. We now detail the missing data points in our variables: 1 GRB has missing data in γ, 1 has missing data in PhotonIndex, 2 have missing data in β, 4 have missing data in log(Peak Flux), 5 have missing data

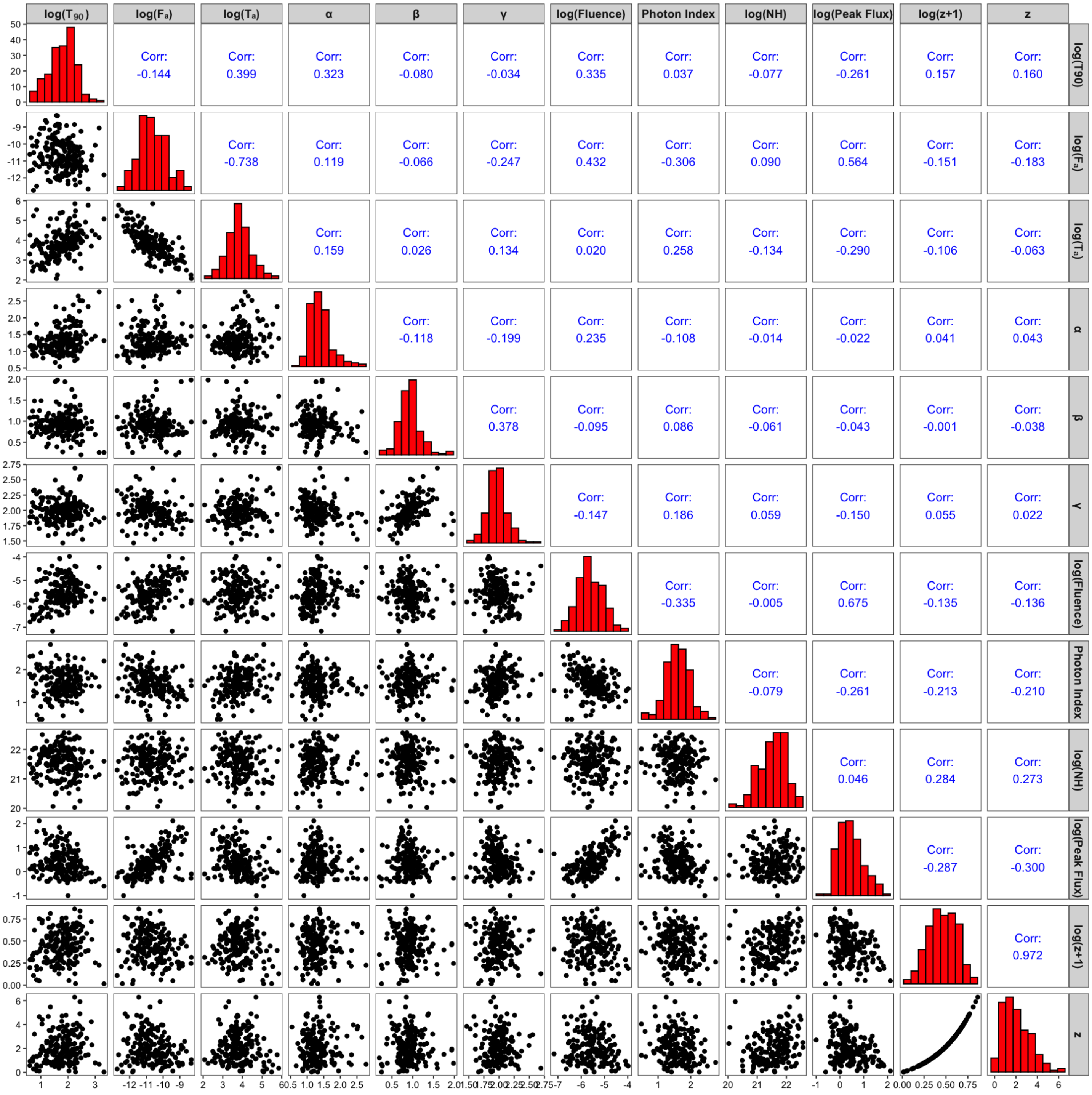

Figure 2. Scatter matrix plot of the data after the cleaning of the sample and variable transformation.

in α, and 17 have missing data in log(NH) While log(T_{90}), log(F_a), log(T_a), and log(Fluence) have no missing data points.

3.2.1. *Nested 10-fold Cross Validation and the Extensive Search*

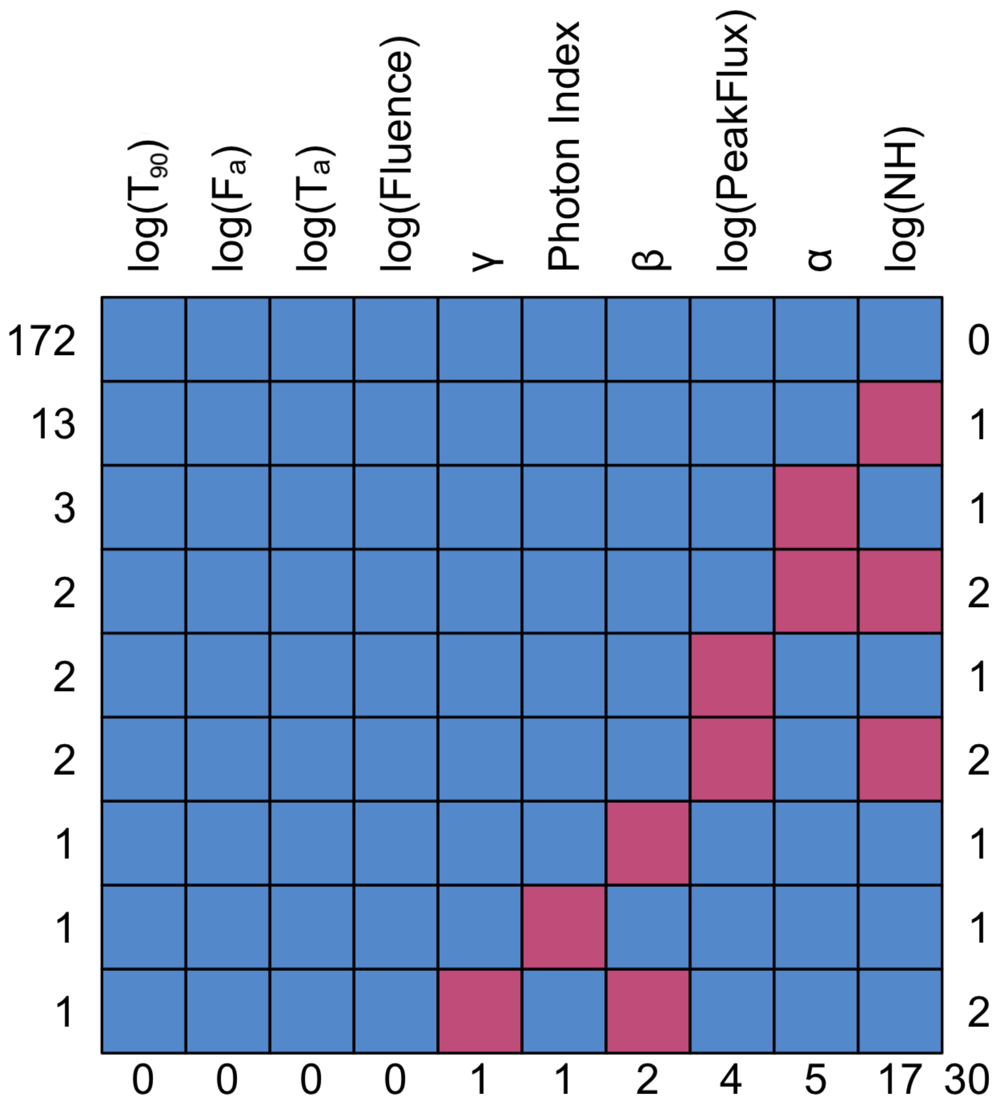

Figure 3. The missing data in our sample. The red boxes show the missing GRB data points, while the blue boxes indicate GRBs with no missing data for a given GRB variable presented in the top axis. The bottom axis shows the number of missing GRBs per variable. The left axis represents the number of observations that have missing data for a specific set of features. For example: there are 172 GRBs with no missing data, 13 GRBs with missing data in log(NH) data, 3 GRBs with missing data in α, and so on. The right axis represents the number of features that are missing for that row.

Here, we describe a nested 100-iteration 10-fold cross-validation (10fCV) procedure that will be utilized in both the outlier removal and model construction stages. This procedure is called nested since it requires an external layer of cross-validation. 10fCV involves dividing our data set into 10 distinct subsets, each containing 10 parts. We then iteratively train the model using 9 out of the 10 subsets as training data and evaluate its performance on the remaining subset as a testing set. This procedure is repeated for each subset, allowing each subset to serve as a testing set, while the others are used for training. We average the prediction results across all the 100 iterations to obtain the mean prediction. The standard deviation of this distribution is the prediction error.

The extensive search we perform uses the nested 100-iteration 10fCV. The procedure preparatory to the extensive search requires first building all possible formula candidates. These formulas are meant for two purposes. The first purpose is generating multiple models for the robust linear model (RLM) using the M-estimator procedure, as explained in Sec. 3.2.2. The second purpose is to create multiple models for both the Generalized Additive Model (GAM) (detailed in Sec. 3.3.2) and the Generalized Linear Model (GLM) (outlined in Sec. 3.3.1), both collectively used to construct the final ensemble method. We build the formulas described above with a generator function that employs the first-order features, which are the observed GRB variables, and the second-order variables, which instead are the multiplicative terms among the first-order variables. Then, the extensive search allows us to find the best formula among all formulas tested based on the correlation between the predicted and observed redshift and the root mean square error (RMSE), a measure of deviation from the model's fit written for N data points as

$$\mathrm{RMSE} = \sqrt{\frac{\sum_{i=1}^{N}(x_i - \hat{x}_i)^2}{N}}, \tag{1}$$

where x_i is the true response value for data point i, and $\hat{x}_i$ is the respective predicted value.

For GAM, RLM, and GLM, each has its own individual cut-off for the correlation and RMSE. This cut allows us to choose the best formulas. Following this, we use these formulas to predict the redshift of the test set. Next, we identify the formula corresponding to the highest correlation, the lowest RMSE, and the lowest median absolute deviation (MAD), which is the median of the absolute difference between each data point and the mean of the dataset given by

$$\mathrm{MAD} = Median(|x_i - \bar{x}|), \tag{2}$$

where x_i are the data points and $\bar{x}$ is the mean of the dataset x. Finally, we select the best formula from these based on the highest weight in the SuperLearner (detailed in Sec 3.3.3)

3.2.2. *Outlier Removal*

In order to remove outliers we use a robust preliminary regression method, M-estimation, which minimizes the residuals in a given model. The application of the M-estimator enables the fit of an RLM on the imputed data. We conduct an extensive search (see Sec. 3.2.1) to find an optimal formula for the RLM that best fits the data.

To this end, we include square terms of one or multiple features of the data to capture potential non-linear relationships between our predictors and the response variable. The chosen model reads as follows:

$$\begin{aligned}\log(1+z) =&((\log(\mathrm{NH}))^2 + (\log(T_{90}))^2 + (\log(T_a))^2 + (\log(F_a))^2 \\ &+ \log(\mathrm{NH}) + \mathrm{PhotonIndex} + \log(T_{90}) + \log(T_a))^2 + \log(F_a) \\ &+ \log(\mathrm{Peak\ Flux}) + (\mathrm{PhotonIndex})^2 + (\log(\mathrm{Peak\ Flux}))^2.\end{aligned} \tag{3}$$

M-estimator is an alternative technique to the ordinary least squares method, which fits the function mentioned above to our data. The ordinary least squares method attempts to minimize the square of the residuals (called the L_2 norm regression) by giving outliers of the data set a higher weight. This significantly affects the results of the regression fit. In contrast, the M-estimator attempts to minimize the sum of a function of residuals. The function chosen for our analysis is the Huber Function (Huber 1964). RLM is used for the detection of highly influential observations. We are using the implementation of RLM as described in the MASS package of R (Venables & Ripley 2002). Data points with weights falling below 0.5 undergo exclusion, a crucial step taken to counterbalance the influence that potentially problematic data points may exert on the model's effectiveness. Following this outlier removal procedure, we eliminate 6 outliers (050826, 051109B, 080916A, 111008A, 151112A, and 160327A), reducing the size of our data set to 191 GRBs.

3.2.3. *Feature Selection*

The preprocessed data is now divided into two sets: an 80% training set for model training and a 20% test set for performance evaluation which is never used for the best model selection. We decide to reduce the number of variables to be investigated, and thus we select the most predictive features given the small data sample. To identify the most important features, we use the Least Absolute Shrinkage and Selection Operator (LASSO) method exclusively on the training set (Tibshirani 1996). To ensure the stability of the results, we perform LASSO for 100 iterations and obtain as a result the averaged weights for each predictor. We here choose as a threshold the average weight value of 0.01 to reduce the number of features. The variables for which the LASSO weight is > 0.01 are chosen as features in Superlearner, (see Fig. 4). From the LASSO process, we extract the top features, including $\log_{10} T_{90}$, $\log_{10} F_a$, $\log_{10} T_a$, PhotonIndex, $\log_{10}$ NH, and $\log_{10}$ Peak Flux. These features will be used in all the successive steps of our analysis to find the most predictive model.

3.3. *Model Construction*

Once the data has been preprocessed, we begin constructing an ensemble of supervised ML algorithms to model the relationships between the GRB features and their corresponding redshifts. Supervised ML leverages prior knowledge of the 'training' data on which ML models will be built, and their predictions will be tested on new data (the 'test' set). Parametric models use functions with a set of parameters whose coefficients are fine-tuned to fit the training data. These models, although simpler and faster to train, are however constrained by the functions. Non-parametric models, in contrast, without assuming a predefined function, are thus more flexible and powerful than parametric methods. However, they are prone to over-fitting, require large samples, and extensive running time. Semi-parametric models have a parametric and a non-parametric component, thus leveraging the advantages of both models.

We begin our construction by testing a total of 115 different regression methods on 10 iterations of 10fCV. These 115 models include the best of the following ML algorithms which were tested individually: Random forest models, with differing numbers of trees, ranging from 10 to 500; extreme gradient boosting models using the same tree combinations. Further, 92 models from the caret package (Kuhn & Max 2008) were also tested. And finally, a single support vector machine (SVM) model was picked from a combination of 7921 models. These combinations were obtained by changing the various hyperparameters of the SVM model.

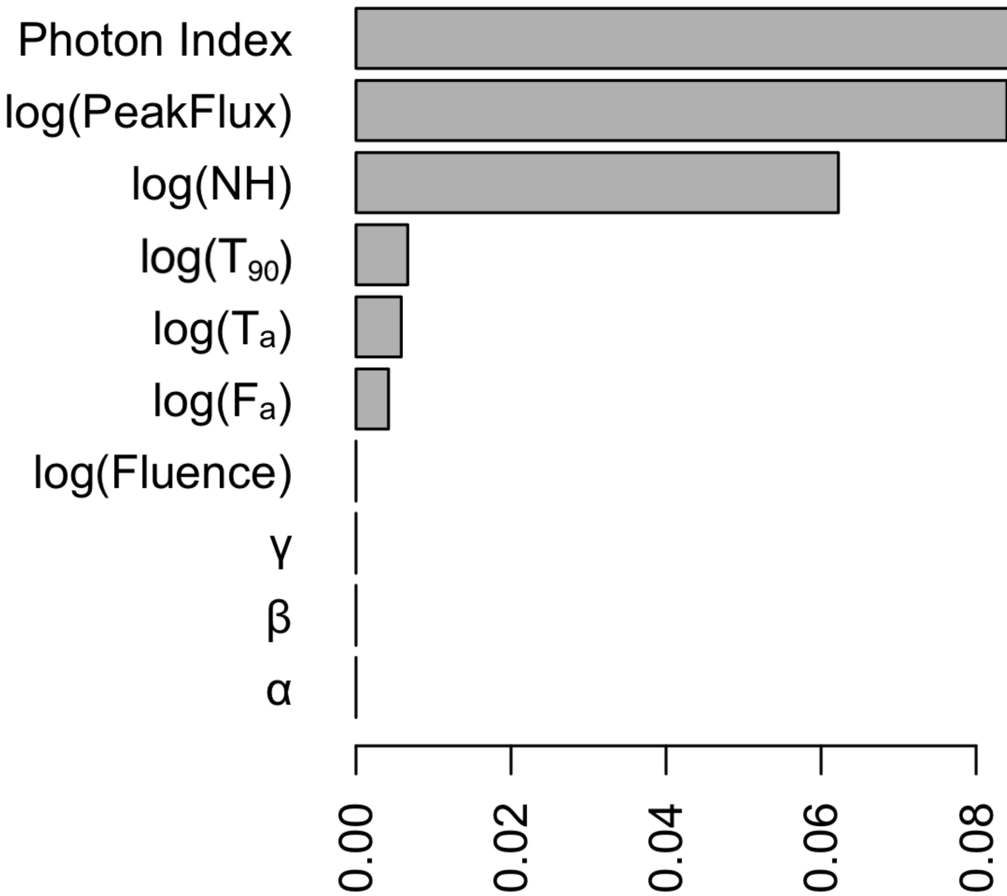

Figure 4. The weights assigned to the features by LASSO.

Out of these 115 models 25 models were selected for obtaining the highest correlation during the surveys. Namely, these were GAM; GLM, Bayesian GLM, GLM Network, and Interaction GLM; Extreme Gradient Boosted trees; Recursive Partitioning and Regression Trees (RPart) and Random Forest as implemented by the caret package; Random Forest with Conditional Inference, R's native RPart, RPart with Pruning, Bagged Trees, Fast Implementation of Random Forest (ranger); Ridge; Stepwise Akaike Information Criterion, Interaction Stepwise Regression, Forward Stepwise Regression, and Classical Stepwise Regression; Feed Forward Neural Network; Regression Towards the Mean; Local Weigthed Regression; Linear Modeling; a tuned Kernel Support Vector Machine; Fast Multivariate Adaptive Regression Splines; and a scalable version of Lasso.

Our search for the best ML models consistently exhibited a preference for linear parametric and semi-parametric models. The resilience of these models leads us to believe that standardizing a tuning methodology for the non-parametric models is not required for this work. As a general remark, we would like to stress that in principle the fully non-parametric models have the advantage of estimating complicated non-linear relationships between the response variable and the predictors as well as high-order interactions between features. Such non-parametric methods are very powerful when the data set contains many observations. However, they suffer from the so-called "curse of dimensionality", which sets limits on the number of parameters one can efficiently estimate for a given sample size. This "curse" becomes more severe with a greater number of features. As a result, the fully non-parametric ML methods allow the use of only a limited number of features, e.g. when estimating redshifts based on small GRB training sets, as in this case.

3.3.1. *The Generalized Linear Model*

GLM is a parametric regression technique that utilizes specialized link functions to relate the distribution of the response variable to a linear combination of the predictors. As opposed to the standard linear model, GLM excels in its ability to handle various distributions, such as Gaussian, Poisson, and Gamma, by selecting the appropriate link function. The model's parameters are estimated through Maximum Likelihood Estimation (MLE), iteratively refined for optimal fit (Nelder & Wedderburn 1972). This allows us to explore different model architectures and identify the most suitable model for our data. We perform the extensive search over 4158 formulae (see the left panel of Fig 5), composed of first and second-order variables. For GLM, the 10fCV cut-offs are $r \geq 0.66$ and $RMSE \leq 0.145$. The formula that obtains the best correlation on the test set (see Sec 3.2.1) is selected as the final formula. In our implementation of GLM, we assign the formula below as the desired fitting function. This is based on our results from the extensive search (see Sec. 3.2.1) with a Gaussian link function:

$$\begin{aligned}\log(1+z) =&((\log(\mathrm{NH}))^2 + (\log(T_{90}))^2 + (\log(T_a))^2 + (\log(F_a))^2 + \log(\mathrm{NH}) \\ &+ \mathrm{PhotonIndex} + \log(T_{90}) + \log(T_a))^2 + \log(F_a) \\ &+ \log(\mathrm{Peak\ Flux}) + (\mathrm{PhotonIndex})^2 + (\log(\mathrm{Peak\ Flux}))^2.\end{aligned} \tag{4}$$

3.3.2. *The Generalized Additive Model*

In the semi-parametric GAM (Hastie & Tibshirani 1990), the redshift is related to the GRB variables via the sum of either parametric or non-parametric functions including smooth functions or a combination of both. The advantage of GAM is that incorporates smooth functions on specified features to relate nonlinear relationships between the features and the response variable. Each of the smooth functions is represented using a group of basis functions, also known as B-splines, which compose a piecewise polynomial function to relate the smoothed predictor to the response, constrained by a specified degree of freedom. In our implementation of GAM, however, a penalty term is applied to the B-splines to penalize high complexity, eliminating the need for manually specifying the degrees of freedom.

Here, we emphasize the significance of utilizing first-order variables, as opposed to second-order variables. The use of second-order variables possesses the following disadvantages: firstly, the error related to the features would be squared and further propagated onto the redshift. In addition, there would be unnecessary complexity added to the model, especially considering that formulas with first-order variables with similar prediction quality exist. For these reasons, by prioritizing first-order variables, we enhance the precision of our predictions and subsequent error estimation. Thus, our extensive search for GAM is conducted on 141 formulae (see the right panel of Fig 5), composed of both smoothed and unsmoothed first-order variables. We employ cuts of $r \geq 0.653$ and $RMSE \leq 0.137$ to narrow down the best formulae for final selection based on performance on the test set (see Sec 3.2.1). We finally arrive at the below-mentioned formula for GAM:

$$\begin{aligned}\log{(1+z)} =&s(\log \mathrm{NH}) + s(\log T_{90}) + s(\log T_a) \\ &+ \log F_a + \mathrm{PhotonIndex} + \log \mathrm{Peak\ Flux}.\end{aligned} \tag{5}$$

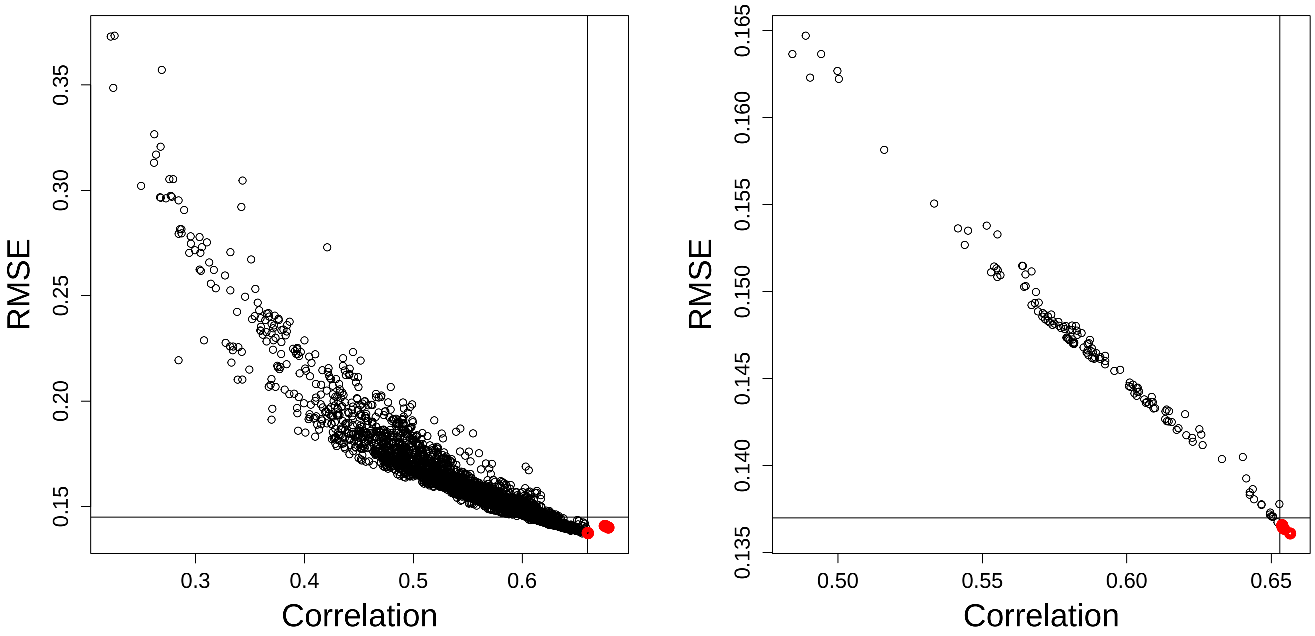

Figure 5. The plot of the cross-validation results of RMSE and the r in the $\log(z+1)$ of GLM (left) and GAM (right) formulae. Each dot on either plot represents a formula performance within the 10fCV. The red dots represent the formulae that were above the chosen RMSE and Correlation.

3.3.3. *SuperLearner*

The SuperLearner is an ensemble of ML models that has the advantage of combining several ML methods into a single model and leveraging the predictive power of each singular model. It is also able to use the same model with varying configurations and asses how each of these models performs. However, to perform this assessment the models must be constructed in such a way as to minimize the anticipated risk, which quantifies the model accuracy, by reducing the RMSE, represented as the square root of the average squared error $\langle \Delta z^2 \rangle$.

Outside of the algorithm, we employ a nested 10fCV 100 times (as mentioned in Sec 3.2.1) to gauge the accuracy of each individual ML model. By analyzing the ensemble's behavior across different runs, we aim to identify the best-performing set of models and their corresponding weights. Subsequently, SuperLearner creates an optimal weighted combination of these models, providing an ensemble based on the performance on the test data. SuperLearner provides coefficients that indicate the weight (A_i) or significance of each individual learner within the collective ensemble. By default, these weights are non-negative and sum to 1. This approach has been demonstrated to lead to the accuracy of the most effective prediction algorithm tested, as an asymptotic outcome.

We survey 115 models individually, as described in Sec. 3.3 and we employ 25. Then, we use weights assigned by SuperLearner as a discriminator among the most predictive models and we remove models weighted < 0.25 after having performed a 100 10fCV to ensure the stability of the most performative models.

3.4. *The relative importance*

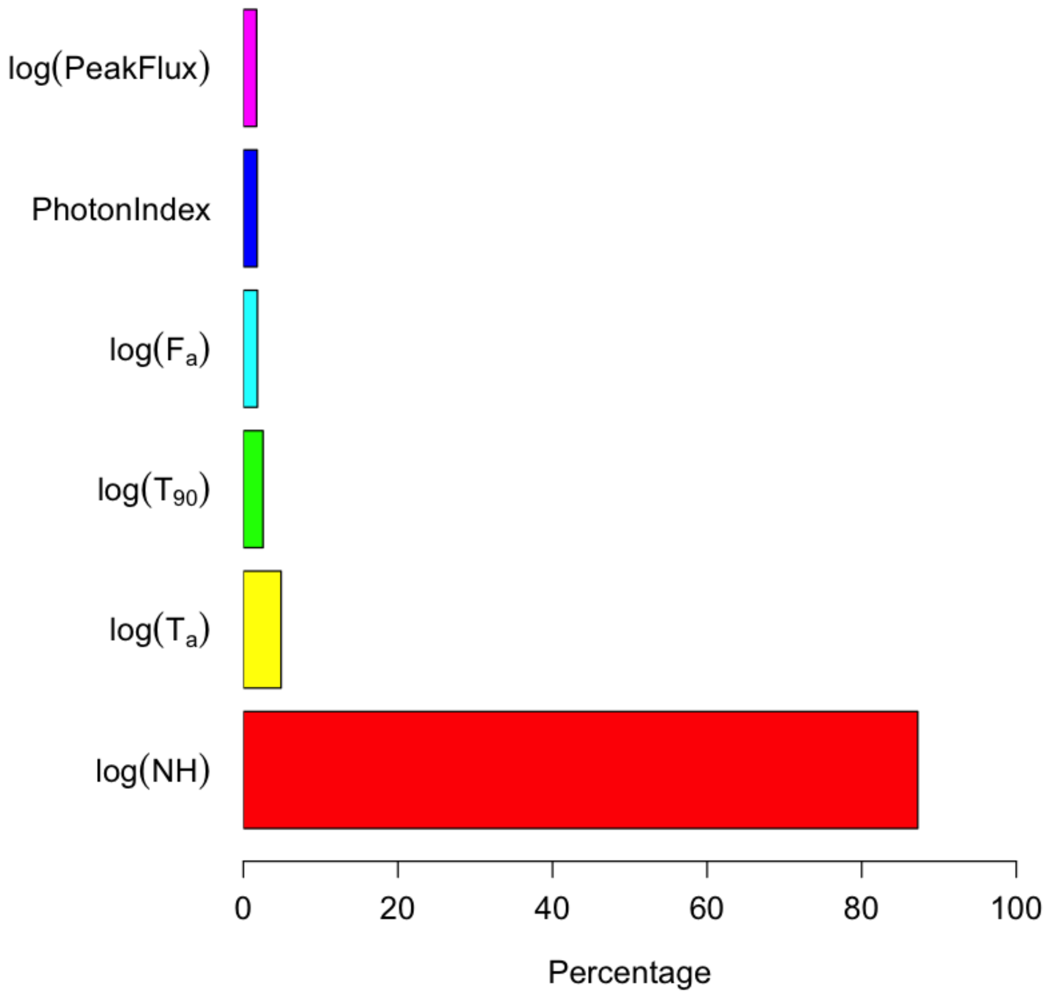

Figure 6. Plot of relative influence of each predictor including in each predictor also the second-order variables.

To assess the contribution of each predictor, we use the relative importance of features which is an average of local importance given by a local linear approximation of prediction. For each observation, synthetic data is generated by adding Gaussian noise. Subsequently, we construct an approximate change in prediction through a linear model prediction, $P = X \times B$ where B are fit coefficients. The local relative importance of feature i is defined by $R_i = |Bi|/P|Bi|$ for all sample points. In Fig. 6, we show the relative influence of the variables where each first order variable contains also the sum also of the second-order variables obtained with the ensemble of several methods. As we can see, the second most important variable is T_a, highlighting the importance of adding the plateau emission among the features. Indeed, all the variables related to the plateau emission survive the trimming performed by LASSO, and these variables, T_a, Peak Flux, and F_a, naturally recover the Dainotti correlation discussed in the Sec. 1.

3.4.1. *Error prediction and the Catastrophic Outlier Removal*

The GRBs in our sample have error measurements for $\log(F_a)$, $\log(T_a)$, T_{90}, Peak flux and PhotonIndex. The uncertainties on $\log(NH)$ are difficult to gather since they are not present in the BAT catalog and for many GRBs such uncertainties are lacking. Thus, in the measurement errors we do not include the $\log(NH)$ uncertainties. In order to account for these observational uncertainties, we perform a Monte-Carlo Markov Chain (MCMC) approach, making the assumption that our uncertainties are Gaussian, because the uncertainties on the variables are independent between measurements of the same variable, and are random.

The error bars on z_{pred} are generated by MCMC simulations with Gaussian distributions centered around the central value of the observed variables and as standard deviation their measurement uncertainties. This procedure is repeated 100 times for each GRB in the 10fCV algorithm and allows to obtain a redshift distribution whose minimum and maximum represent the error bars on z_{pred}, see the errorbars in the Fig. 7.

We obtain the 1σ and 2σ cones in Fig. 7 between z_{pred} and z_{obs}. The 1-σ and 2 σ are defined as:

$$1\sigma = 10^{\sigma^*} z + (10^{\sigma^*} - 1)$$

$$2\sigma = 10^{2\sigma^*} z + (10^{2\sigma^*} - 1)$$

where σ^* is the standard deviation in the $\log_{10}(z+1)$ scale.

It is at this stage that we remove additional outliers deemed to be 'catastrophic'. These catastrophic outliers are defined in Jones & Singal (2020) as the GRBs which $|\Delta z| > 2\sigma$. In our case, these catastrophic outliers are 9, and as shown in Fig. 7, they fall outside of the blue cone. Following this additional outlier removal procedure, our sample of 151 GRBs is reduced to 143 GRBs. It is important to note that we do not retrain our models following the catastrophic outlier removal.

3.4.2. *Bias Correction*

Following the removal of catastrophic outliers, we perform bias correction on our predictions. Bias is defined as the mean of the difference between predicted and observed values of the response variable. When training models on an imbalanced sample or a sample that has some level of discrimination against a set of random variable outcomes, the model's predictions can have significant bias. With an imbalanced sample, the model becomes more skilled at predicting the redshift range with more observations. To correct for this bias, we use the Optimal Transport bias correction technique. This involves sorting in ascending order the predicted and observed values and fitting a linear model between them. The bias is corrected using the slope and intercept of this fit following this formula:

$$Y_{pred} = \beta_0 + \beta_1 Y_{SL}$$

where Y_{preds} is the corrected predictions, Y_{SL} is the SuperLearner predictions, and β_0 and β_1 are the intercept and slope of the linear fits, respectively. Solving for the fitted Y_{pred} values provides the bias-corrected redshift estimates. We apply this technique separately to four independent regions, namely, $z_{obs} < 2$, $2 < z_{obs} < 3.5$, $3.5 < z_{obs} < 5.0$, and $z_{obs} > 5.0$. It results in a correlation $r = 0.93$, $RMS = 0.46$ and bias=0.0031. This allows us to adapt the bias correction to different ranges of z_{obs}, providing more accurate results.

3.4.3. *Predicting the redshift of the Generalization Set*

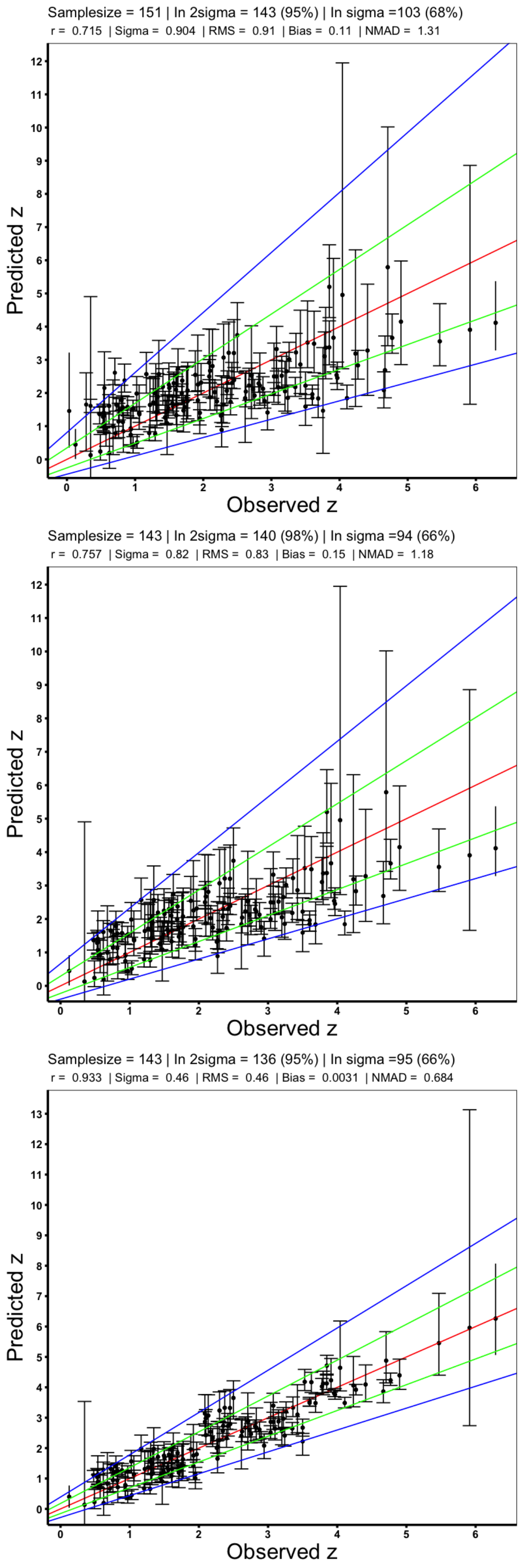

Figure 7. The scatter plot between z_{obs} and z_{pred}. Upper panel: Predictions before removal of catastrophic outliers and bias correction. Middle panel: Predictions after the removal of catastrophic outliers. Lower panel: Predictions after the removal catastrophic outliers and application of bias correction.

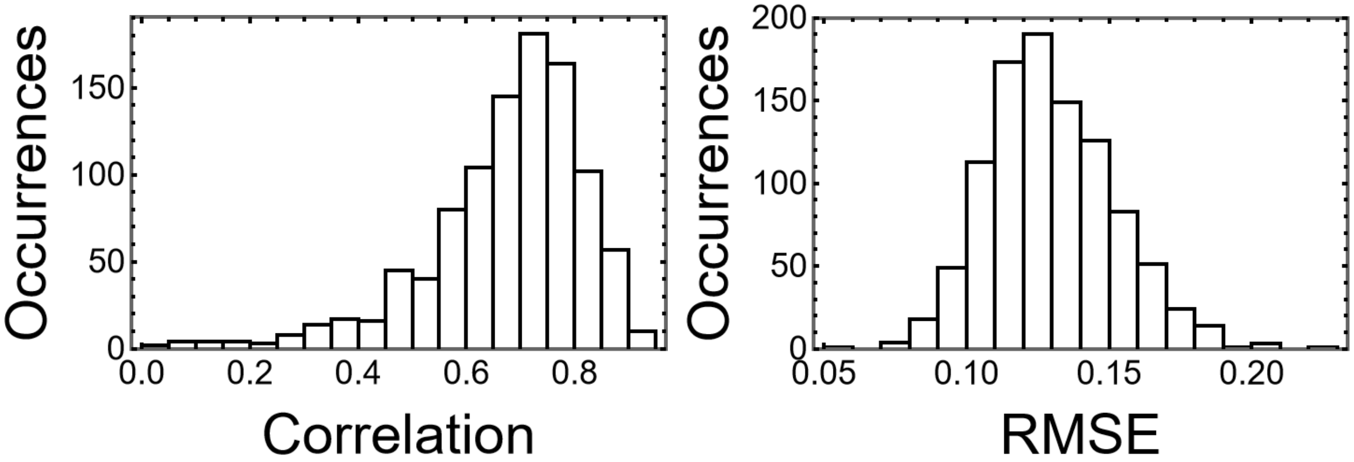

Figure 8. Histograms of our chosen metrics on testing sets. Both correlation and RMSE are computed in the $\log(z+1)$ scale. Left panel: correlation between predicted and observed redshift. Right panel: RMSE of the predicted redshifts.

Given that our model has been fully validated in 3.2.1, we may now begin making predictions for our generalization set. With the best model obtained with the SuperLearner, we predict the redshift using the same predictors we have used in the training set. Since there is no observed redshift data for this dataset, we check that our predicted redshifts come from the same parent population of the observed redshifts. We perform the Kolmogrov-Smirnov test (Karson 1968) and Anderson-Darling test (Stephens 1974) to verify if the two sets of data share the same underlying distribution.

4. RESULTS

In this section, we present the results of our analysis, including the performance of GAM, GLM, and the SuperLearner ensemble. We also discuss the implications of our findings and the application of these models in estimating the redshift in the generalization set.

4.1. *Performance Metrics and Comparison*

The benchmark for evaluating the quality of our results revolves around minimizing the RMSE within the SuperLearner algorithm. To further evaluate the efficacy of our results, we also utilize the following metrics in conjunction with SuperLearner RMSE: the Pearson correlation coefficient (r) between z_{obs} and z_{pred}, the normalized median absolute deviation (NMAD), and the bias defined as the expectation $\langle z_{pred} - z_{obs} \rangle$. These metrics provide a reliable assessment of each model's ability to predict redshift values accurately.

4.2. *SuperLearner Results*

The Superlearner identified GAM and GLM as the best predicting models. The ensemble generated with GAM, $A_1 = 0.655$, exhibits the highest predictive capability, followed by GLM ($A_2 = 0.345$). In this context, A_1 and A_2 denote coefficients indicating the optimal model and reflecting the weighted average of multiple models.

The results obtained from SuperLearner are presented in Fig. 7. We obtain a r=0.715, RMSE=0.91, bias=0.11 and NMAD=1.31 between z_{obs} and z_{pred} including all GRBs. The catastrophic outlier percentage is 6%. Following the steps mentioned in Sec. 3.4.1 and Sec. 3.4.2, the results after the catastrophic outliers are removed ar shown in the middle panel of Fig. 7. Here we obtain an improvement of the correlation which reach $r = 0.756$, a RMS=0.83 and a bias=0.15. The bias-corrected results are presented in the bottom panel of Fig. 7. Here we see an improvement compared to the results non-biased corrected and including the catastrophic outliers. The improvement is visible in all the metrics: r=0.93 (21% increase), RMSE=0.46 (45% decrease) and NMAD=0.68 (63% decrease) between z_{obs} and z_{pred}. The catastrophic outlier percentage also drops from 5.3% to 4.9%. For high-z GRBs ($z_{obs} \geq 3$), r=0.88, marking a 54% increase in correlation, MSE=0.23, and bias=0.16.

4.3. *GAM and GLM Performance*

We begin by evaluating the predictive performance of the GAM and GLM models individually. We identified the most promising formulas for each model based on cross-validation metrics, specifically correlation, RMSE, and MAD. We found that the selected formulas for both GAM and GLM models demonstrated substantial correlation (0.66 and 0.64, respectively) in $\log(z{+}1)$ and exhibited relatively low RMSE (0.99 and 1.20) and MAD (1.41 and 1.30) values when performed on 100 10fCV. The GAM and the GLM formulae that perform the best in terms of correlation are quoted in Eq. 5 and Eq. 4, respectively.

Results of SuperLearner on the test sets during 10fCV are presented in Fig. 8, which shows the distribution of r (left panel) and the RMSE (right panel) of the 100 runs of the nested-fold 100fCV procedure. Our results show that the accuracy of the prediction is quite stable with a correlation coefficient between the z_{pred} vs. z_{obs} which peaks at 70 and an RMSE which peaks at 0.13 for the majority of partitions in the training sets and test sets. However, for a small number of partitions, we observe a small correlation coefficient and a higher MSE. This is indeed natural due to the large heterogeneity of the data and the relatively small sample size.

4.4. *Predicting the Generalized Data Set*

The distributions of the predicted and z_{obs} are presented in Fig. 10 with dashed and solid lines, respectively, indicated inside the figure as training and generalization sets. The generalization set distribution has been obtained using the model after the optimal transport bias correction. We have checked the Anderson Darling for these two distribution and the hypothesis that they are drawn by the same parent population is rejected. We further investigate the reason why the two distributions are not compatible with each other and we investigated the distribution of each variable that comes into play. We observed that the distributions of two variables ($\log(T_{90}$ and $\log(NH)$) are also not drawn by the same parent population according to the Anderson Darling Test. Thus, possibly this is the cause of this discrepancy. In addition, in our initial sample we have removed the intrinsically SGRBs (15 GRBs), but since the intrinsically SGRBs need to have a redshift to be defined, we do not have the possibility to highlight them. Another problem is that the classification of the short GRBs with extended emission for GRBs without redshift is not often reported in the literature and thus it is hard in the generalization to classify GRBs appropriately for this task. In order for us to further investigate this issue we have then added the IS to the sample and we have repeated the same procedure described above. We note that the best GAM model and the best GLM are the same as the ones detailed in the previous sections.

We have computed both the prediction errors and the errorbars on the predictions following the approach detailed in Sec. 3.4.1. The contribution of these error bars are shown in the boxplot presented in Fig. 9. It is clear for some GRBs the error measurements are large, but overall we can assess that our method is reliable to infer the redshift for GRBs for which the redshift is unknown. Indeed, in this box plot there is a GRB (110801A) for which the prediction of the redshift is < 0, which is not included in the plot and additional 3 GRBs (GRB 110414, 150817A, GRB 090518) included in the plot for which the errorbars on T_{90} are larger than the measurement of T_{90} itself. [We need to substitute the Figure 9]

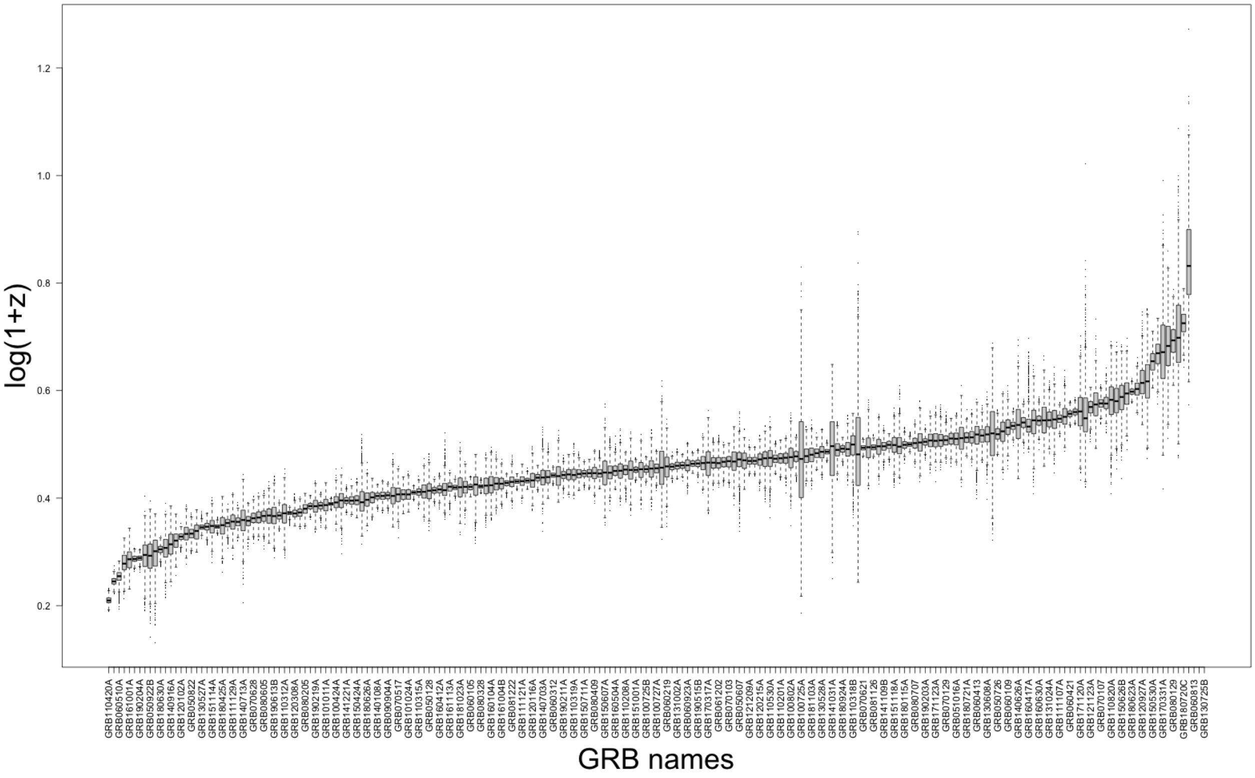

Figure 9. The box plot for each GRB is shown for the generalization set. The error bars are shown for each prediction.

4.4.1. *Comparative Results*

Prior to our investigation, several groups have used linear or non-linear relations between relevant GRB parameters. However, the redshift inferred with these methods has not yet led to accurate measurements (Reichart 2001; Yonetoku et al. 2004; Atteia 2005). Even when the inferred redshift uncertainty is small (5%), these measurements are provided only for a few cases (Guiriec et al. 2016). When the redshift is inferred from the correlation between the peak in the νF_ν spectrum, E_{peak}, and the energy emitted isotropically (Amati et al. 2002) during the prompt emission, r obtained between z_{obs} and z_{pred} is 0.67 (Atteia 2003). These z_{pred} estimates, tested on 17 GRBs, are accurate only by a factor of 2 (Amati 2006). When the redshift is inferred from the bi-dimensional X-ray Dainotti correlation between L_a and $T_a/(1+z)$, only 28% of cases have small errorbars, namely $(z_{pred} - z_{obs})/z_{obs} < 1$ (Dainotti et al. 2011). All these attempts are parametric.

Compared to Ukwatta et al. (2016), parameters like prompt duration, Photon Index, fluence, and hydrogen column density remain the same. Thus, it is the plateau variables, used here for the first

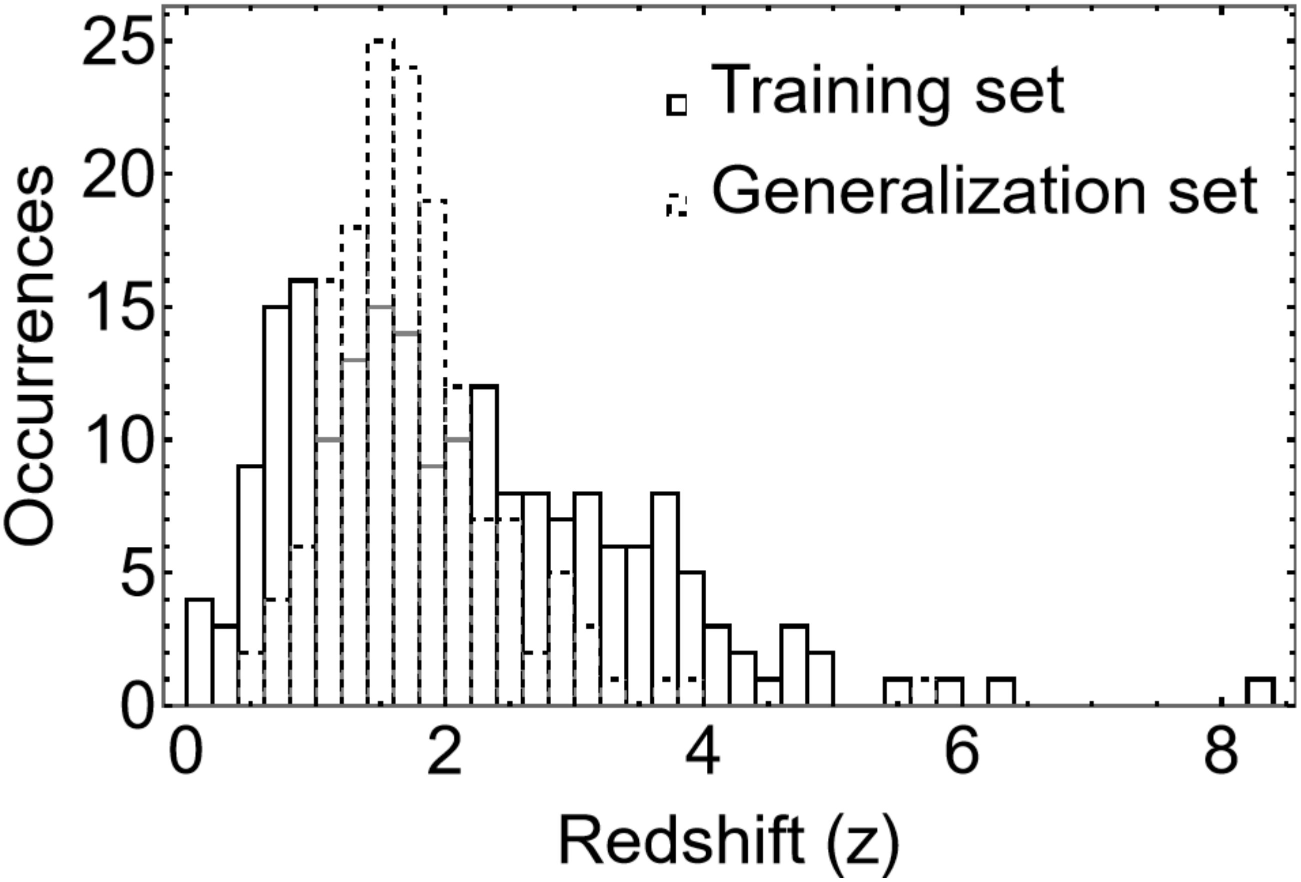

Figure 10. Histogram comparing the distributions of the training set z_{obs} and the redshift predictions of the generalization set.

time, that greatly enhance the results. Indeed, our $r = 0.93$ after bias correction leads to a 63% rise in correlation compared to Ukwatta et al. (2016).

The novel solution proposed here uses supervised ML algorithms to infer redshift from many GRB variables, including the plateau emission, with a combination of parametric and semi-parametric methods. Previously, Ukwatta et al. (2016) employed Random Forest to estimate redshifts using prompt parameters, obtaining a small correlation between z_{pred} and z_{obs} (r=0.57). Thus, we have a 60% increase in the correlation compared to these previous results. Crucially, unlike prior works, we have included here the plateau features. Another problem, hardly explored in the literature (besides our study), is to account for measurement errors of GRB variables used to train ML models. Further, comparing our results with Racz et al. (2017), who achieved a r=0.67, we see a 22% increase in our correlation in the $\log_{10}(z+1)$ scale when we apply the bias-correction. In addition, our methodology is more complete than this work, since we use the LASSO feature selection, the M-estimator, the nested 100-10fCV, the Superlearner and the bias correction. Furthermore, we performed an extensive search by minimizing the RMSE and maximizing the correlations. All these steps have not been performed in the mentioned proceeding.

5. SUMMARY, DISCUSSION AND CONCLUSION

In this paper, we have developed a methodology to predict the redshift of GRBs from the Swift catalogue using prompt, plateau and afterglow parameters derived from the BAT+XRT observations. The steps we have followed are:

1. Cleaning and imputing the missing variables with MICE;
2. Removing the outliers using an M-estimator;
3. Applying the LASSO method to select the most predictive feature to reduce the number of predictors given the small data sample;
4. Using the SuperLearner to perform a nested 10fCV method on 25 different models to determine which models would be the most successful.
5. We determine that our best ML models for the ensemble are GAM and GLM;
6. Optimizing each model by performing an extensive search aimed to maximize the Pearson Correlation coefficient and minimize RMSE on a test data;
7. Creating our final ensemble with Eq. 5 for GAM and Eq. 4 for the GLM.
8. Performing a 4-way bias correction on our training set predictions.
9. Predicting the redshifts for the generalization set, including their prediction errors and the estimated observational uncertainties on the predicted redshifts. This is achieved using MCMC simulations based on the uncertainties on the variables (see Sec. 4.4).

In comparison to other attempts to infer GRB redshift, our ensemble achieves an increase of 63% and 38% in the correlation between predicted and observed redshift reaching $r = 0.93$, compared to other works in which only random forest or gradient boosting alone were used. Ukwatta et al. (2016) found $r = 0.57$ with random forest, while Rácz et al. (2017) found $r = 0.67$ both with random forest and gradient boosting. The main difference, besides our enhanced prediction and the fact that we use a more complete methodology which has been detailed in Sec. 3, is the use of the plateau properties.

In this work we highlight that the use of ML techniques for redshift prediction in GRBs offers several advantages over the commonly used parametric methods which employs only the use of bidimensional relations. Our individual GAM and GLM models exhibit strong predictive capabilities and demonstrate how to surpass the accuracy of existing approaches. In general, our study has shown that the use of parametric and semi-parametric methods brings an enhanced performance compared to the fully non-parametric approaches, like random forest, which are more prone to overfitting compared to our methods. In addition, the advantage for the parametric and semi-parametric models are more interpretable than the non-parametric models. We have also shown that improved performance are actually happening with a reduced set of variables which contain first-order terms exclusively.

Further, our study is a proof of concept for utilizing GRBs as standard candles in cosmology with the newly estimated redshifts from the generalization set. We have indeed increase the sample size of GRBs with known redshift by adding 208 GRBs (we have 420 GRBs with redshift so far) by 50% of the total sample of GRBs with redshift. With this new number we can use the Dainotti relation to serve as reliable cosmological tool. If we consider then, the increase of the estimates of GRBs with X-ray plateus then the increase is of 94%.

Looking towards the future, this is a preparatory work which will allows us to find values of Ω_M with a similar precision as Conley et al. (2011). As discussed in Dainotti et al. (2022a), we would require 789 GRBs with X-ray plateaus to reach such a precision if we use GRBs which possess X-ray plateaus (see Table 9 in Dainotti et al. (2022b)). Since in the current analysis we obtain 147 GRBs with unknown redshift and X-ray plateaus, we currently have a sample of 222+147=369 GRBs with redshifts both known and inferred. Since we have a yearly rate of 15 GRBs with X-ray plateaus observed with redshift and 15 observed without redshift our sample can be incremented from August 2019 until August 2023 of additional 120 GRBs. This means that once we analyze the available GRBs with plateaus we will have 489 GRBs with known and inferred redshift. This will leave us only to wait for 789-489=300 GRBs to be observed which with a rate of 30 GRBs with X-ray plateaus per year, will be reached in roughly 10 years. However, if we apply the lightcurve reconstruction analysis Dainotti et al. (2023) we will have an higher precision on the plateau parameters (on average 37.5%) which will allow us to need less GRBs, namely 37.2% less of the initial total sample as detailed in Dainotti et al. (2022a). Therefore, from the total sample of 789 we should remove its 37.2% which is 293 GRBs. Thus, we would need 496, out of these we have already 489. This leaves us to wait only half a year to then reach the precision of Conley et al. (2011). Thus, with the aid of both ML and lightcurve reconstruction we can aim at an increased precision for cosmology reaching a higher precision, the one obtained by Betoule et al. (2014). For this analysis we would need 987 GRBs, as detailed in Dainotti et al. (2022a), so 987-489=498 GRBs more that can be observed in roughly 18 years. However, if we consider the uncertainties of the parameters of the plateaus divided by half the number of GRBs needed will be almost half of this sample, so the precision of Betoule et al. (2014) can be reached only in 9 years.

In conclusion, this work successfully predict the redshifts of GRBs with X-ray plateau emission, and introduces a pipeline of data processing techniques for obtaining reproducible and reliable results. Through preprocessing, imputation, model selection, and performance evaluation, we predict redshifts for 147 of LGRBs.

Our results is a proof-of-concept showing the potential of ML-based methods to enhance the field of astrophysics, and cosmology. By expanding the dataset of GRBs with known redshifts we can successfully tackle population studies such as the more accurate estimate of the luminosity function and density rate evolution enabling a deeper understanding of the high-z universe and its evolution. As further data becomes available and ML techniques continue to evolve, the accuracy and precision of redshift predictions for GRBs are likely to improve, offering exciting prospects for future cosmological research.

6. ACKNOWLEDGMENTS

We acknowledge Artem Poliszczuk for the discussion about the extensive search. We acknowledge funding from Swift GI Cycle XIX, grant number 22-SWIFT22-0032. This work was also supported by the Polish National Science Centre grant UMO-2018/30/M/ST9/00757 and by Polish Ministry of Science and Higher Education grant DIR/WK/2018/12.

REFERENCES

Ajello, M., Arimoto, M., Axelsson, M., et al. 2019, ApJ, 878, 52, doi: 10.3847/1538-4357/ab1d4e

Amati, L. 2006, Monthly Notices of the Royal Astronomical Society, 372, 233, doi: 10.1111/j.1365-2966.2006.10840.x

Amati, L., Frontera, F., Tavani, M., et al. 2002, Astronomy and Astrophysics, 390, 81, doi: 10.1051/0004-6361:20020722

Atteia, J.-L. 2003, Astronomy &amp Astrophysics, 407, L1, doi: 10.1051/0004-6361:20030958

—. 2005, Il Nuovo Cimento C, 28, 647–652, doi: 10.1393/ncc/i2005-10120-7

Bargiacchi, M., Dainotti, M., & Capozziello, S. 2023, MNRAS

Barthelmy, S. D., Barbier, L. M., Cummings, J. R., et al. 2005, Space Science Reviews

Beskin, G., Karpov, S., Bondar, S., et al. 2010, The Astrophysical Journal Letters, 719, L10, doi: 10.1088/2041-8205/719/1/L10

Betoule, M., Kessler, R., Guy, J., et al. 2014, Astronomy &amp Astrophysics, 568, A22, doi: 10.1051/0004-6361/201423413

Burrows, D. N., Hill, J. E., Nousek, J. A., et al. 2005, Space Science Reviews, 120, 165, doi: 10.1007/s11214-005-5097-2

Cao, S., Dainotti, M., & Ratra, B. 2022a, Monthly Notices of the Royal Astronomical Society, 512, 439, doi: 10.1093/mnras/stac517

—. 2022b, Monthly Notices of the Royal Astronomical Society, 516, 1386, doi: 10.1093/mnras/stac2170

Cao, S., Khadka, N., & Ratra, B. 2021, Monthly Notices of the Royal Astronomical Society, 510, 2928, doi: 10.1093/mnras/stab3559

Cardone, V. F., Capozziello, S., & Dainotti, M. G. 2009, MNRAS, 400, 775, doi: 10.1111/j.1365-2966.2009.15456.x

Cardone, V. F., Dainotti, M. G., Capozziello, S., & Willingale, R. 2010, MNRAS, 408, 1181, doi: 10.1111/j.1365-2966.2010.17197.x

Conley, A., Guy, J., Sullivan, M., et al. 2011, ApJS

Costa, E., Frontera, F., Heise, J., et al. 1997, Nature, 387, 783, doi: 10.1038/42885

Cucchiara, A., Levan, A. J., Fox, D. B., et al. 2011, The Astrophysical Journal

Dainotti, M., Levine, D., Fraija, N., & Chandra, P. 2021, Galaxies, 9, 95, doi: 10.3390/galaxies9040095

Dainotti, M. G., Bargiacchi, G., Bogdan, M., Capozziello, S., & Nagataki, S. 2023, Reduced uncertainties up to 43% on the Hubble constant and the matter density with the SNe Ia with a new statistical analysis, arXiv, doi: 10.48550/ARXIV.2303.06974

Dainotti, M. G., Bargiacchi, G., Łukasz Lenart, A., et al. 2022a, The Astrophysical Journal, 931, 106, doi: 10.3847/1538-4357/ac6593

Dainotti, M. G., Cardone, V. F., & Capozziello, S. 2008, Monthly Notices of the Royal Astronomical Society, 391, L79, doi: 10.1111/j.1745-3933.2008.00560.x

Dainotti, M. G., Del Vecchio, R., Shigehiro, N., & Capozziello, S. 2015, ApJ, 800, 31, doi: 10.1088/0004-637X/800/1/31

Dainotti, M. G., Fabrizio Cardone, V., Capozziello, S., Ostrowski, M., & Willingale, R. 2011, The Astrophysical Journal, 730, 135, doi: 10.1088/0004-637X/730/2/135

Dainotti, M. G., Hernandez, X., Postnikov, S., et al. 2017, The Astrophysical Journal, 848, 88, doi: 10.3847/1538-4357/aa8a6b

Dainotti, M. G., Hernandez, X., Postnikov, S., et al. 2017, The Astrophysical Journal, 848, 88

Dainotti, M. G., Lenart, A. , Chraya, A., et al. 2022b, APJ. https://arxiv.org/pdf/2209.08675.pdf

Dainotti, M. G., Ostrowski, M., & Willingale, R. 2011, Monthly Notices of the Royal Astronomical Society, 418, 2202, doi: 10.1111/j.1365-2966.2011.19433.x

Dainotti, M. G., Petrosian, V., Singal, J., & Ostrowski, M. 2013, The Astrophysical Journal, 774, 157, doi: 10.1088/0004-637x/774/2/157

Dainotti, M. G., Petrosian, V., Singal, J., & Ostrowski, M. 2013, ApJ, 774, 157, doi: 10.1088/0004-637X/774/2/157

Dainotti, M. G., Postnikov, S., Hernandez, X., & Ostrowski, M. 2016, The Astrophysical Journal Letters, 825, L20, doi: 10.3847/2041-8205/825/2/L20

Dainotti, M. G., Sharma, R., Narendra, A., et al. 2023, ApJS, 267, 42, doi: 10.3847/1538-4365/acdd07

Dainotti, M. G., Via Nielson, G. S., Rinaldi, E., et al. 2022c, Galaxies, 514, 1828, doi: 10.3390/galaxies10010024

Dainotti, M. G., Livermore, S., Kann, D. A., et al. 2020, ApJL, 905, L26, doi: 10.3847/2041-8213/abcda9

Dainotti, M. G., Livermore, S., Kann, D. A., et al. 2020, The Astrophysical Journal Letters, 905, L26, doi: 10.3847/2041-8213/abcda9

Dainotti, M. G., Omodei, N., Srinivasaragavan, G. P., et al. 2021, ApJS, 255, 13, doi: 10.3847/1538-4365/abfe17

Efron, B., & Petrosian, V. 1992, ApJ, 399, 345, doi: 10.1086/171931

Evans, P. A., Beardmore, A. P., Page, K. L., et al. 2009, Monthly Notices of the Royal Astronomical Society, 397, 1177, doi: 10.1111/j.1365-2966.2009.14913.x

Galama, T. J., Vreeswijk, P. M., & Paradijs, J. V. 1998, Nature

Gehrels, N., Chincarini, G., Giommi, P., et al. 2004, The Astrophysical Journal, 611, 1005, doi: 10.1086/422091

Gibson, S. J., Narendra, A., Dainotti, M. G., et al. 2022, Frontiers in Astronomy and Space Sciences, 9, doi: 10.3389/fspas.2022.836215

Gorbovskoy, E. S., Lipunova, G. V., Lipunov, V. M., et al. 2012, Monthly Notices of the Royal Astronomical Society, 421, 1874, doi: 10.1111/j.1365-2966.2012.20195.x

Guiriec, S., Gonzalez, M. M., Sacahui, J. R., et al. 2016, The Astrophysical Journal, 819, 79, doi: 10.3847/0004-637X/819/1/79

Hastie, T., & Tibshirani, R. 1990, Generalized Additive Models (Routledge), doi: https://doi.org/10.1201/9780203753781

Huber, P. J. 1964, The Annals of Mathematical Statistics, 35, 73 , doi: 10.1214/aoms/1177703732

Jones, E., & Singal, J. 2020, Publications of the Astronomical Society of the Pacific, 132, 024501

Kann, D. A., Klose, S., & Zeh, A. 2006, The Astrophysical Journal, 641, 993, doi: 10.1086/500652

Karson, M. 1968, Journal of the American Statistical Association, 63, 1047, doi: 10.1080/01621459.1968.11009335

Kuhn, & Max. 2008, Journal of Statistical Software, 28, 1–26, doi: 10.18637/jss.v028.i05

Levine, D., Dainotti, M., Zvonarek, K. J., et al. 2022, The Astrophysical Journal, 925, 15, doi: 10.3847/1538-4357/ac4221

Li, L., Wu, X.-F., Lei, W.-H., et al. 2018, The Astrophysical Journal Supplement, 236, 26, doi: 10.3847/1538-4365/aabaf3

Liang, E.-W., Zhang, B.-B., & Zhang, B. 2007, The Astrophysical Journal, 670, 565, doi: 10.1086/521870

Lien, A., Sakamoto, T., Barthelmy, S. D., et al. 2016, The Astrophysical Journal, 829, 7, doi: 10.3847/0004-637x/829/1/7

Little, R. J., & Rubin, D. B. 2019, Statistical analysis with missing data, Vol. 793 (John Wiley & Sons)

Narendra, A., Gibson, S. J., Dainotti, M. G., et al. 2022, The Astrophysical Journal Supplement Series, 259, 55, doi: 10.3847/1538-4365/ac545a

Nelder, J., & Wedderburn, R. 1972, Journal of the Royal Statistical Society. Series A, 135, 370, doi: https://doi.org/10.2307/2344614

Norris, J. P., & Bonnell, J. T. 2006, The Astrophysical Journal, 643, 266, doi: 10.1086/502796

Nousek, J. A., Kouveliotou, C., Grupe, D., et al. 2006, The Astrophysical Journal, 642, 389, doi: 10.1086/500724

Oates, S. R., Page, M. J., De Pasquale, M., et al. 2012, Monthly Notices of the Royal Astronomical Society, 426, L86, doi: 10.1111/j.1745-3933.2012.01331.x

O'Brien, P. T., Willingale, R., Osborne, J., et al. 2006, The Astrophysical Journal, 647, 1213, doi: 10.1086/505457

Panaitescu, A., & Vestrand, W. T. 2008, Monthly Notices of the Royal Astronomical Society, 387, 497, doi: 10.1111/j.1365-2966.2008.13231.x

—. 2011, Monthly Notices of the Royal Astronomical Society, 414, 3537, doi: 10.1111/j.1365-2966.2011.18653.x

Petrosian, V., Kitanidis, E., & Kocevski, D. 2015, The Astrophysical Journal, 806, 44, doi: 10.1088/0004-637x/806/1/44

Piro, L., Amati, L., Antonelli, L. A., et al. 1998, Astronomy and Astrophysics, 331, L41. https://arxiv.org/abs/astro-ph/9710355

Postnikov, S., Dainotti, M. G., Hernandez, X., & Capozziello, S. 2014, ApJ, 783, 126, doi: 10.1088/0004-637X/783/2/126

Racz, I. I., Ribli, D., Bagoly, Z., et al. 2017, in Proceedings of the 7th International Fermi Symposium, 79

Rácz, I. I., Ribli, D., Bagoly, Z., et al. 2017, in Proceedings of 7th International Fermi Symposium — PoS(IFS2017) (Sissa Medialab), doi: 10.22323/1.312.0079

Reichart, D. E. 2001, The Astrophysical Journal, 554, 643, doi: 10.1086/321428

Rodney, S. A., & Riess, A. G. 2015, AJ

Roming, P. W. A., Kennedy, T. E., Mason, K. O., et al. 2005, Space Science Reviews, 120, 95, doi: 10.1007/s11214-005-5095-4

Rowlinson, A., Gompertz, B. P., Dainotti, M., et al. 2014, Monthly Notices of the Royal Astronomical Society, 443, 1779, doi: 10.1093/mnras/stu1277

Sakamoto, T., Hill, J. E., Yamazaki, R., et al. 2007, The Astrophysical Journal, 669, 1115, doi: 10.1086/521640

Scolnic, D. M., Jones, D. O., Rest, A., et al. 2018, The Astrophysical Journal, 859, 101, doi: 10.3847/1538-4357/aab9bb

Srinivasaragavan, G. P., Dainotti, M. G., Fraija, N., et al. 2020, The Astrophysical Journal, 903, 18, doi: 10.3847/1538-4357/abb702

Stephens, M. A. 1974, Journal of the American Statistical Association, 69, 730, doi: 10.1080/01621459.1974.10480196

Tanvir, N. R., Fox, D. B., & Levan, A. J. 2008, Nature

Tibshirani, R. 1996, Journal of the Royal Statistical Society, 58, 267

Ukwatta, T. N., Woźniak, P. R., & Gehrels, N. 2016, Monthly Notices of the Royal Astronomical Society, 458, 3821, doi: 10.1093/mnras/stw559

Ukwatta, T. N., Woźniak, P. R., & Gehrels, N. 2016, Monthly Notices of the Royal Astronomical Society, 458, 3821, doi: 10.1093/mnras/stw559

van Paradijs, J., Groot, P. J., Galama, T., et al. 1997, Nature, 386, 686, doi: 10.1038/386686a0

Venables, W. N., & Ripley, B. D. 2002, in Modern applied statistics with S (Springer), 271–300

Vestrand, W. T., Wozniak, P. R., Wren, J. A., et al. 2005, Nature, 435, 178, doi: 10.1038/nature03515

Vestrand, W. T., Wren, J. A., Panaitescu, A., et al. 2014, Science, 343, 38, doi: 10.1126/science.1242316

Yonetoku, D., Murakami, T., Nakamura, T., et al. 2004, The Astrophysical Journal, 609, 935, doi: 10.1086/421285

Zaninoni, E., Bernardini, M. G., Margutti, R., Oates, S., & Chincarini, G. 2013, Astronomy and Astrophysics, 557, A12, doi: 10.1051/0004-6361/201321221

Zeh, A., Klose, S., & Kann, D. A. 2006, The Astrophysical Journal, 637, 889, doi: 10.1086/498442

Zhang, B., Fan, Y. Z., Dyks, J., et al. 2006, The Astrophysical Journal, 642, 354, doi: 10.1086/500723